Nuclear Instruments and Methods in Physics Research A 664 (2012) 264–271

Contents lists available at SciVerse ScienceDirect

Nuclear Instruments and Methods in Physics Research A

journal homepage: www.elsevier.com/locate/nima

Measurement of K_L^0 flux at the J-PARC neutral-kaon beam line

K. Shiomi [a], K.Y. Baek [b], J. Comfort [c], E. Iwai [d], N. Kawasaki [a], J.W. Ko [e], T.K. Komatsubara [f], J.W. Lee [d], G.Y. Lim [f], Y. Maeda [a], T. Masuda [a], D. Naito [a], Y. Nakaya [d,1], H. Nanjo [a], T. Nomura [f,*], M. Sasaki [g], N. Sasao [h], K. Sato [d], T. Shimogawa [i], Y. Sugiyama [d], Y. Tajima [g], G. Takahashi [a], M. Togawa [d], H. Watanabe [f], T. Yamanaka [d], Y. Yanagida [d], H.Y. Yoshida [g]

[a] *Department of Physics, Kyoto University, Kyoto 606-8502, Japan*
[b] *Department of Physics, Pusan National University, Busan 609-735, South Korea*
[c] *Department of Physics, Arizona State University, Tempe, AZ 85287-1504, USA*
[d] *Department of Physics, Osaka University, Toyonaka, Osaka 560-0043, Japan*
[e] *Department of Physics, Jeju National University, Jeju 690-756, South Korea*
[f] *High Energy Accelerator Research Organization (KEK), Ibaraki 305-0801, Japan*
[g] *Department of Physics, Yamagata University, Yamagata 990-8560, Japan*
[h] *Research Core for Extreme Quantum World, Okayama University, Okayama 700-8530, Japan*
[i] *Department of Physics, Saga University, Saga 840-8502, Japan*

ARTICLE INFO

Article history:
Received 7 October 2011
Received in revised form
31 October 2011
Accepted 4 November 2011
Available online 12 November 2011

Keywords:
K_L^0 production
J-PARC

ABSTRACT

We describe the K_L^0 flux measurements performed at the J-PARC neutral-kaon beam line. This beam line was constructed for an experiment aiming to observe the CP-violating rare decay $K_L^0 \to \pi^0 \nu\bar{\nu}$. The primary proton energy was 30 GeV and the K_L^0 production angle was 16°. Prior to the physics run, the K_L^0 flux and spectrum were measured by counting $K_L^0 \to \pi^+\pi^-\pi^0$ decays with a simple setup, which was composed of an electromagnetic calorimeter and a hodoscope system. Results from these measurements are presented and compared with various hadron-interaction simulations.

1. Introduction

The study of CP violation has been attracting special interests in particle physics because it may provide us with clues to new physics beyond the Standard Model (SM) and the keys for solving the puzzle of the imbalance of matter and anti-matter in the universe. One attractive channel to study CP violation is the rare decay, $K_L^0 \to \pi^0 \nu\bar{\nu}$ [1]. The branching ratio is proportional to η^2 in the SM, where η is the Wolfenstein parameter [2] representing the magnitude of CP violation in quark mixing with three generations [3]. Theoretically, this channel is clean; its branching ratio is predicted to be 2.4×10^{-11} with uncertainties of only a few percent [4]. Thus, precise measurements can either confirm the SM or reveal deviations that in turn are signs of new physics beyond the SM. Experimentally, however, the measurement is challenging because of the extremely small branching ratio. The current upper limit of the branching ratio is 2.6×10^{-8} (90% C.L.), as given by the KEK-E391a experiment [5].

With the advent of the Main Ring (MR) accelerator of the Japan Proton Accelerator Research Complex (J-PARC) [6], the KOTO experiment, now under construction, will probe the $K_L^0 \to \pi^0 \nu\bar{\nu}$ decay down to the SM sensitivity [7]. We have built a new neutral-kaon beam line in 2009, and conducted various beam survey experiments.

The results of K_L^0 flux measurements are described in this paper. There are two motivations for measuring the K_L^0 flux in a separate experiment prior to the physics run. First, various simulation programs predict the K_L^0 fluxes at this beam line that differ by up to a factor of three, and precise knowledge on the K_L^0 yield as well as its momentum spectrum is essential to evaluate the sensitivity of the KOTO experiment. Second, in the physics run, the flux will be determined by measuring $K_L^0 \to \pi^0\pi^0$ with cross-checks by the $K_L^0 \to \pi^0\pi^0\pi^0$ and $K_L^0 \to \gamma\gamma$ decays. All of these are neutral decay modes; it is desirable to check them against a charged decay mode.

The decay mode we have measured is $K_L^0 \to \pi^+\pi^-\pi^0$. This mode was chosen because its branching ratio is large and all decay products can be easily detected, allowing reliable event reconstruction. For the measurement, a simple setup with an electromagnetic calorimeter to detect photons and a hodoscope system to track charged pions was constructed. To fully reconstruct a K_L^0

---

[*] Corresponding author. Tel.: +81 29 879 6052.
E-mail address: nomurat@post.kek.jp (T. Nomura).
[1] Deceased.

0168-9002/$ - see front matter © 2011 Elsevier B.V. All rights reserved.
doi:10.1016/j.nima.2011.11.010

decay without any magnetic spectrometer, equations for the transverse momentum balance of $\pi^+\pi^-\pi^0$ were solved to derive the momenta of the charged pions.

This paper is organized as follows. Section 2 describes the neutral beam line and the experimental apparatus. Sections 3 and 4 describe the analysis procedure and its results in detail. The last section is devoted to the summary.

2. Experiment

2.1. Beam line

We begin this section by describing the neutral-kaon beam line. Details including the design philosophy, parameter choices based on Monte Carlo simulations, the fabrication and installation processes, are reported elsewhere [8,9].

Fig. 1 shows a layout of the beam line and the definition of our coordinate system.

A 30-GeV primary proton beam, extracted from the MR accelerator, was injected into the production target (Ni or Pt). The beam-on time (spill length) was about 2 s in every 6-s cycle. The length of the target along the primary proton beam was 5.4 cm for Ni and 6.0 cm for Pt, respectively.

Secondary particles produced at 16° in the target were channeled to the experimental area which started 20.6 m downstream of the target. The beam went through several beam-line components before it reached the experimental area. First, the beam passed through a 7-cm-thick lead photon absorber, which was used to reduce the number of photons in the beam. Second, it went through a pair of beam collimators to shape the beam. The neutral beam was shaped to be rectangular, and its solid angle was 7.8 μsr. The collimators were designed to reduce the number of "halo neutrons", which were the accompanied neutrons around the beam. The reduction of halo neutron rates was the key issue in designing the beam line because they constituted one of the major sources of the backgrounds to the $K_L^0\to\pi^0\nu\bar{\nu}$ decay in the KEK-E391a experiment [5]. Charged particles in the beam were swept out by a 2-T magnet placed between the two collimators.

In the design stage, several simulation packages of hadron interactions were used to estimate the K_L^0 flux and its momentum distribution. The simulation tools included GEANT4 with the QGSP-BERT-CHIPS physics list [10], GEANT3 with the GFLUKA hadron package [11], and FLUKA [12]. Each code employs different hadronic models and extrapolating/interpolating algorithms to predict the cross-sections of K_L^0 production at a designated energy and angle. In particular, different predictions for large production angles are expected [13]. The resultant K_L^0 fluxes are summarized in Table 1. As shown in the table, they differ from each other by as much as a factor of three, with little difference in their momentum distributions. For reference, we also show the expected neutron and photon fluxes in the table.

2.2. Experimental setup

The experimental setup for the $K_L^0\to\pi^+\pi^-\pi^0$ measurement is shown in Fig. 2. It consisted of two major components to detect $K_L^0\to\pi^+\pi^-\pi^0$ decays from the upstream region of the setup. One component was an electromagnetic calorimeter with undoped CsI crystals to detect photons from π^0 decays. The other component was a tracking system with sets of hodoscope planes to detect charged particles. A bag filled with helium gas (not shown in Fig. 2) was inserted in the beam region between the exit window of the beam line and the surface of the calorimeter to reduce backgrounds due to neutron interactions in the beam. No detectors were placed in the neutral beam in order to avoid excessively high counting rates.

Table 1
K_L^0 flux estimation in the case of Ni target with various simulation packages. Neutron and photon fluxes are also shown for reference. All of the flux values were counted at the exit of the beam line and were normalized to 2×10^{14} primary protons on the target, which corresponds to the designed intensity in a spill from the MR. The 7-cm-thick lead absorber was assumed to be inserted in the beam line.

Package name	K_L^0 flux	Neutron flux ($T_n > 100$ MeV)	Photon flux ($E_\gamma > 10$ MeV)
GEANT4	7.4×10^6	3.2×10^8	5.9×10^7
GEANT3	1.5×10^7	3.8×10^8	5.1×10^7
FLUKA	2.1×10^7	3.7×10^8	7.1×10^7

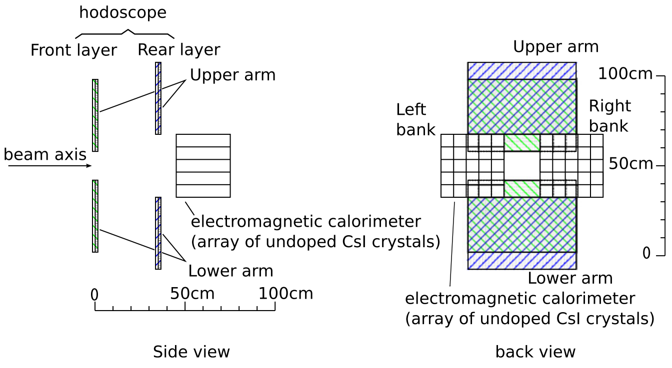

Fig. 2. Schematic drawing of the experimental setup in the side view (left) and the back view (right).

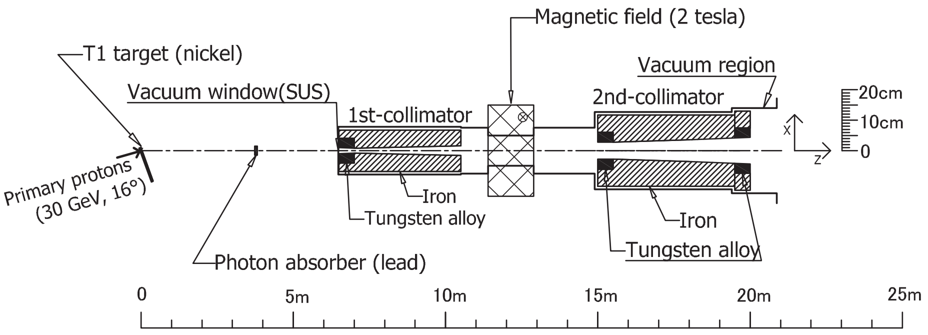

Fig. 1. Schematic layout of the neutral-kaon beam line. It consists of a pair of collimators and a sweeping magnet (2 T). A 7-cm-thick lead absorber is inserted in the beam line to reduce photons. Also shown is the coordinate system used in this paper: x in the horizontal, y in the vertical, and z in the beam directions. The origin of the coordinate is set at the center of the production target. The exit window of the beam line (not shown) is located at z=20.6 m.

2.3. CsI calorimeter

As shown in Fig. 2, there were two calorimeter banks: one was located on the left and the other on the right side of the beam with a 20-cm space between the two. A bank consisted of 25 undoped CsI crystals, each being $7\times7\times30\,\mathrm{cm}^3$ and stacked in a 5×5 matrix. Hamamatsu R4275-02 photomultiplier tubes (PMTs) [14] were used to readout scintillating light from the crystals. All of the PMTs and the crystals were acquired from the calorimeter used in the E391a experiment [15]. These PMTs were attached to the downstream end of the crystals and their signals were sent to a subsequent readout system. The front faces of the calorimeter banks were covered with plastic scintillators to detect and veto charged particles hitting the calorimeter.

The gain of each calorimeter module was calibrated in situ with cosmic rays during the runs, and was refined by multiplying an overall factor so that a peak position in the invariant mass distribution of two photons, which is discussed later, became consistent with the nominal π^0 mass. The energy and timing resolutions were measured in a test experiment by using a portion of the calorimeter (nine crystals). These measurements, carried out with positrons with the energies between 200 and 800 MeV, resulted in the energy resolution of 1.9% and the timing resolution of 0.4 ns at 800 MeV. Parameters of the CsI calorimeter are listed in Table 2.

Table 2
Parameters of the electromagnetic calorimeter. There were two banks, located left and right sides of the beam.

Item	Description
Number of crystals	25 per bank, arranged in the 5×5 matrix
Crystal size	$7\times7\times30\,\mathrm{cm}^3$
Crystal material	Undoped CsI
z-Position	z=24.1 m (at the front surface)
Transverse coverage	$35\times35\,\mathrm{cm}^2$ in each bank $10\le|x|\le45$ cm, $|y|\le17.5$ cm
Readout photomultiplier	Hamamatsu R4275-02

2.4. Tracking hodoscope

Charged particles were detected by a set of plastic-scintillator hodoscopes. As shown in Fig. 2, they consisted of two identical arms, one above and the other below the beam, which were designated as the upper and lower arms, respectively. Each arm consisted of two hodoscope layers: the front and rear layers separated by ~35 cm in the beam direction. Each of the hodoscope layers was composed of x and y planes that measure the horizontal and vertical positions, respectively. Each plane was an array of 1-cm-wide and 0.5-cm-thick scintillator strips (ELJEN EJ230 [16]) with wavelength-shifting (WLS) fibers (Kuraray B2 [17]) grooved into the strips.

All WLS fibers were viewed by multi-anode PMTs (Hamamatsu H8804). Their gains were calibrated with cosmic rays and were monitored by light-emitting-diodes (LEDs). The timing resolution was found to be better than 1.4 ns, which was measured in the same test experiment as that for the calorimeter. Parameters of the tracking hodoscope are listed in Tables 3 and 4.

Table 3
Structure and dimensions of the tracking hodoscope. There were two identical arms: upper and lower arms, as shown in Fig. 2. Labels x and y indicate the planes which measured x and y position, respectively.

Item	Description
Front plane	
z-Position	z=23.65 m $\Delta z_{cal}=-44.7$ cm from the calorimeter
Transverse coverage	$60\times40\,\mathrm{cm}^2$ in each arm $|x|\le30$ cm, $8\le|y|\le48$ cm
Strip size	1-cm-wide, 0.5-cm-thick
Number of strips	60 (x), 40 (y)
Rear plane	
z-Position	z=24.00 m $\Delta z_{cal}=-10.0$ cm from the calorimeter
Transverse coverage	$60\times40\,\mathrm{cm}^2$ in each arm $|x|\le30$ cm, $17.5\le|y|\le57.5$ cm
Strip size	1-cm-wide, 0.5-cm-thick
Number of strips	60 (x), 40 (y)

Table 4
Components of the tracking hodoscope. Labels x and y indicate the planes which measured the x and y positions, respectively.

Item	Description
Plastic scintillator	ELJEN EJ230
Thickness	5 mm
Wavelength shifting fibers	Kuraray B2
Diameter	1.5 mm ϕ
Number of fibers	1 per strip
Readout	
Photomultiplier	8×8 multi-anode, Hamamatsu H8804
Configuration	From single end (x) From both ends (y)

2.5. Data acquisition system and trigger

2.5.1. Data acquisition system

Raw signals from the PMTs in the calorimeter were fed into "amplifier-and-discriminator" (A&D) modules, which were originally developed for the KEK E391a experiment. Each A&D module accepted eight analog inputs from the PMTs and produced three types of outputs: buffered analog signals ($1\times$ amplified), discriminated logic signals (with the energy threshold of 1 MeV) for the individual inputs, and a linear sum of the eight inputs. The analog signals were sent to CAMAC analog-to-digital converter (ADC) modules, while the logic signals were routed to VME multi-hit time-to-digital converter (MHTDC) modules. The linear sum signal was used in a trigger logic circuit described later.

Raw signals from the hodoscopes were fed into custom readout equipment that incorporated VA/TA chips [18]. Four (eight) VA/TA chips were used for each x (y) plane. Each VA/TA chip produced two types of outputs: a serialized voltage signal corresponding to the individual input charges, and a timing signal (TA timing signal). The former output was sent to a custom VME module and was digitized by a 12-bit flash ADC. The latter output was an OR logic signal of inputs, whose discrimination thresholds were set at voltages equivalent to one photo-electron. It was split into two, and they were sent to the MHTDC module and the trigger logic circuit, respectively. Digitized data were collected into a computer via both CAMAC and VME systems.

2.5.2. Trigger

Several types of triggers were formed in this experiment. With the physics trigger, we collected events with two photons hitting two calorimeter banks and two pions hitting two hodoscope arms. A hit in the calorimeter bank was defined as an energy deposit of more than 20 MeV. More precisely, 25 signals from one calorimeter bank were divided into four groups, and at least one A&D sum signal among the four groups was required to exceed the 20-MeV threshold. On the other hand, a hit in the hodoscope

Table 5
Chronology of data taking runs. "POT" means the number of protons on the target.

Date	Target	Accumulated POT	Number of triggers	MR power (kW)
2010/02/17–18	Ni	4.9×10^{15}	1.4×10^{4}	1.0
2010/02/19	Ni	7.9×10^{15}	2.3×10^{4}	1.5
2010/02/19–20	Pt	1.5×10^{16}	9.9×10^{4}	1.0
2010/02/20–22	Ni	1.6×10^{16}	4.5×10^{4}	1.0

required at least one TA timing signal in a single plane. As mentioned earlier, the threshold for the TA timing signal was set at the one photo-electron level, which was equivalent to the energy deposit of 0.04–0.06 MeV. The trigger timing was determined by the coincidence between two hits from calorimeter banks. In the data taking runs, the trigger rate was 1.2–3.3 Hz, depending on the primary proton intensity.

In addition to the physics trigger, we prepared a cosmic-ray trigger and an LED trigger to calibrate and monitor the calorimeter and scintillator gains, and a clock trigger to monitor the ADC pedestals.

2.6. Data taking

Data were collected over several days in February 2010, with each run being one-day or two-days long. The chronology of the data taking runs is shown in Table 5. There are two distinct sets of runs: one used the Ni target and the other used the Pt target. The data reported in this paper corresponds to 2.9×10^{16} protons on the Ni target and 1.5×10^{16} protons on the Pt target. Each run was analyzed separately, and then the runs with the same target were combined. We concentrate on the Ni target data in the following sections, and only quote results for the Pt target data.

3. Data analysis

3.1. Primary event selection

The first step in the analysis was to identify good hits in each hodoscope plane and in the calorimeter bank. A good hit in the hodoscope satisfied the following conditions:

- An energy deposit must be larger than 0.25 times the energy deposited by the passage of a minimum ionizing particle (E_{mip}).
- The hit timing must lie within ± 79 ns of the event timing.

The E_{mip} for the 0.5-cm-thick scintillators was 1 MeV, corresponding to 21 (14) photo-electrons for the $x(y)$ planes. The event timing was determined by the trigger timing from the coincidence signal of the two calorimeter banks, as stated in the previous section.

Next, the following conditions for a good hit in the calorimeter bank were imposed:

- The total energy deposit in each bank must exceed 50 MeV, where the total energy was calculated by summing all signals in the bank within the time window of ± 79 ns.
- There must be no hit in the charge veto plastic scintillators in front of the calorimeter, where a hit was defined as a signal larger than $0.4\times E_{mip}$ within the 500-ns-wide ADC gate.

After selecting good hits, the hit positions and track positions in the hodoscope were calculated. The hit position in each hodoscope plane was defined as the center of the strip with a hit, or the center of the strips if there were multiple hits adjacent to each other. The x and y track positions were determined in each layer. If there were more than two hits in a single plane, all x–y combinations were retained for further analysis. The fraction of the events with multiple hits was found to be 29–35%, depending on the beam condition.

Next, two track positions in the front and rear layers were connected to obtain a straight line as a track candidate. The candidates were required to be diverging from the beam, expecting good tracks to originate from the upstream beam region. With two track candidates from the upper and lower arms, the closest distance between two tracks (d_{min}) were calculated. If there were more than one track candidates in one arm due to multiple hits, the combination with the smallest d_{min} was selected. The vertex position (x_v, y_v, z_v) was then defined as the center of the points on two tracks which gave d_{min}. At this point, d_{min} was required to be less than 5 cm. In addition, the transverse vertex position (x_v, y_v) should satisfy the conditions $|x_v|<8$ cm and $|y_v|<8$ cm, which corresponded to the beam size in the experimental setup.

The final step in the primary event selection was to determine the photon momenta. The hit position of a photon at the calorimeter surface was defined as the center-of-energy position of all (5×5) energy deposits in a bank. The direction of a photon was obtained by connecting the vertex point to the hit position. With information on the total energy in each bank, the momentum vector of each photon was reconstructed. As the results of all of these steps, $\pi^{\pm}$ track candidates, their vertex position, and the momentum vectors of two photons were obtained.

3.2. Kinematical selection

Before discussing the kinematical selection, the Monte Carlo (MC) simulation for the detector system is described. The simulations were based on the GEANT4 package. They included various K_L^0 decay processes, interactions of decay products with the detector materials, and response of the detectors. They also treated neutrons in the beam. The neutrons interacted with various materials or residual gas molecules in the beam region and produced false signals in the detector. Both the simulated data (MC data) and the real data were analyzed with the same analysis code. The MC results are presented together with the results from the real data.[2]

In the analysis of $K_L^0\to\pi^+\pi^-\pi^0$ decays, we first calculated the invariant mass of two photons ($M_{\gamma\gamma}$). Fig. 3 shows the $M_{\gamma\gamma}$ distribution, with a peak observed at the nominal π^0 mass. Backgrounds from other K_L^0 decays in the low mass region were dominated by $K_L^0\to\pi e\nu$ and $K_L^0\to\pi\mu\nu$ decays with charged pions hitting the support structure of the detector and producing hadronic showers that faked photons in the calorimeter. Small contributions from $K_L^0\to3\pi^0$ decays with a π^0 dalitz decay also remained over a broad mass region. Backgrounds due to neutron interactions were found to be negligible (and are not plotted in the figure). To select events with a π^0, the two-photon invariant mass was required to satisfy the condition $105<M_{\gamma\gamma}<165\ \mathrm{MeV}/c^2$. In the following, we assume these two photons originate from a π^0 and denote their summed momentum by p_0. The $\pi^{\pm}$ momenta were then calculated. To do that, momentum conservation in the plane perpendicular to the K_L^0 direction was imposed to the transverse momentum balance of the $\pi^+\pi^-\pi^0$ system. Referring

---

[2] The resultant K_L^0 flux and spectrum by this study were used as the inputs of the simulation.

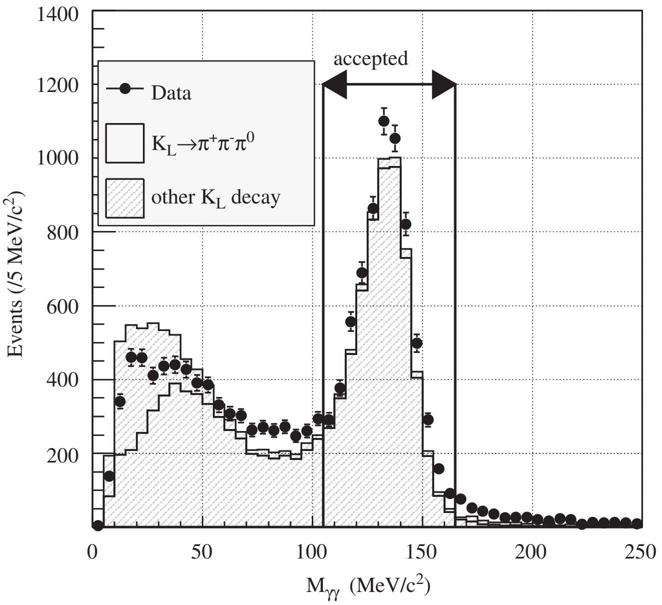

Fig. 3. Invariant mass distribution of two photons after the primary event selection described in Section 3.1. Dots with bars indicate the data. Histograms show the $K_L^0 \to \pi^+\pi^-\pi^0$ signals (open) and backgrounds from K_L^0 decays (hatched), respectively, from the simulation results. Events between the two lines were accepted as π^0-inclusive events.

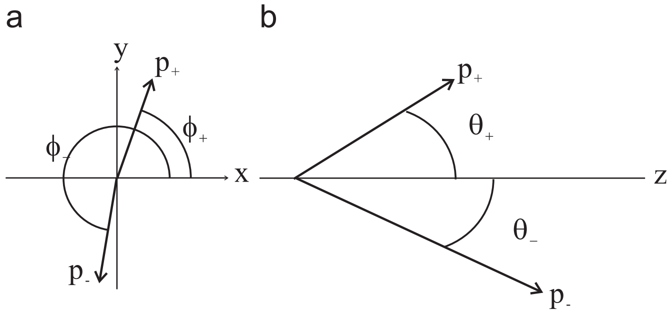

Fig. 4. Notation of the (a) transverse and (b) longitudinal components of the $\pi^\pm$ momentum vectors.

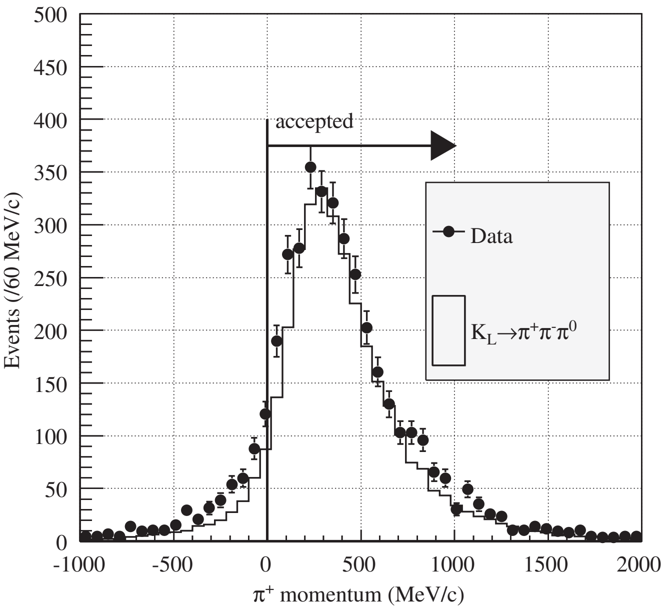

Fig. 5. Sample of the π^+ momentum distribution after the kinematical cuts on $M_{\gamma\gamma}$ and $\phi_\pm$. Here, the charge "+" indicates the track passed through the upper arm of the hodoscope. Dots with bars indicate the data and a histogram shows the $K_L^0 \to \pi^+\pi^-\pi^0$ signals from the simulation result. The contributions from backgrounds were found to be negligible and were not overlaid hereafter.

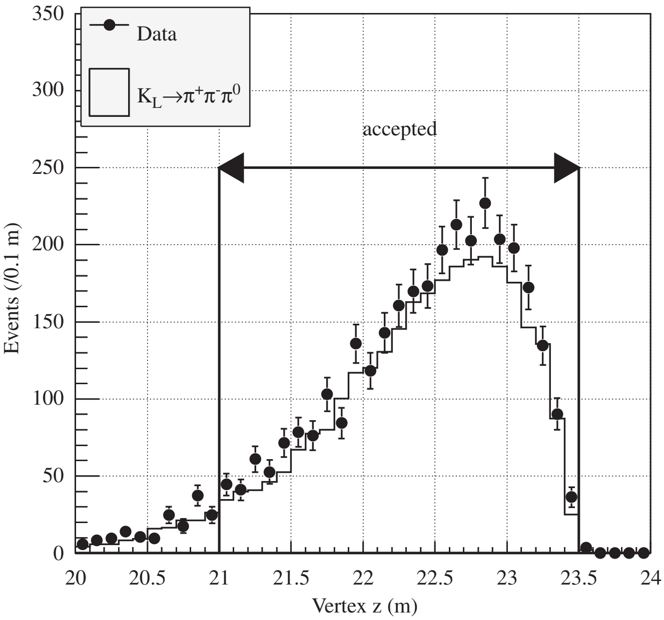

Fig. 6. Vertex distribution after the kinematical cuts on $M_{\gamma\gamma}$, $\phi_\pm$, and $p_\pm$. Dots with bars indicate the data and a histogram shows the $K_L^0 \to \pi^+\pi^-\pi^0$ signals from the simulation result. The range between two lines indicates the fiducial region.

to Fig. 4, the transverse momentum conservation is represented as

$$p_+ \sin\theta_+ \cos\phi_+ + p_- \sin\theta_- \cos\phi_- + p_{0x} = 0 \quad (1)$$

$$p_+ \sin\theta_+ \sin\phi_+ + p_- \sin\theta_- \sin\phi_- + p_{0y} = 0 \quad (2)$$

where $p_\pm$, $\theta_\pm$ and $\phi_\pm$ are the absolute momentum and the polar and azimuthal angles of $\pi^\pm$, respectively, and $p_{0x}(p_{0y})$ denotes the x(y) component of the π^0 momentum. Here in the analysis, the K_L^0 direction was assumed to be identical to the z direction since the solid angle of the beam was small. In the equations, tracks in the upper and lower arms were designated as π^+ and π^-, respectively.

In Eqs. (1) and (2), the unknown variables are $p_\pm$, and these are obtained without ambiguity. However, if the directions of the π^+ and π^- happened to be collinear in the x–y plane, i.e. $\phi_- = 180^\circ + \phi_+$,[3] then Eqs. (1) and (2) are linearly dependent, making them impossible to solve for $p_\pm$. To avoid that, only those events that satisfied $|\Delta\phi_\pm| < 168^\circ$ or $|\Delta\phi_\pm| > 192^\circ$ were selected, where $\Delta\phi_\pm = \phi_+ - \phi_-$. Fig. 5 shows a sample of the $\pi^\pm$ momentum distribution. Both p_+ and p_- were required to be positive, as shown in Fig. 5.

Further cuts were applied to ensure the events to be in the fiducial region of the detectors. Fig. 6 shows the z_v distribution obtained at this stage.

We required z_v to be in the range $21.0 < z_v < 23.5$ m ($-3.1 < \Delta z_v < -0.6$ m from the front surface of the calorimeter). We also required the distance between two photons ($d_{2\gamma}$) in the calorimeter to be larger than 40 cm.

Finally we constructed the invariant mass of π^+, π^- and π^0 ($M_{\pi^+\pi^-\pi^0}$). The result is shown in Fig. 7, where a K_L^0 peak is

---

[3] Because two tracks were required to pass through the upper and lower hodoscopes, another collinear condition $\phi_+ = \phi_-$ should not happen.

observed with negligible background contamination. We identified those events that satisfied $460 < M_{\pi^+\pi^-\pi^0} < 540\ \mathrm{MeV}/c^2$ as K_L^0. After imposing all the cuts, the observed number of K_L^0 decays was 1923 for the Ni target. Table 6 summarizes the numbers of remaining events after various kinematical cuts. For the Pt target runs, the same analysis procedure was taken and 2217 events passed all the cuts.

The background contamination was studied by MC simulations and found to be 0.5% (0.5%) from the $K_L^0 \to 3\pi^0$ and 0.3% (0.6%) from neutron interactions in the beam region in the case of the Ni (Pt) target. In the discussion of the K_L^0 flux below, these backgrounds were subtracted from the observed numbers of events.

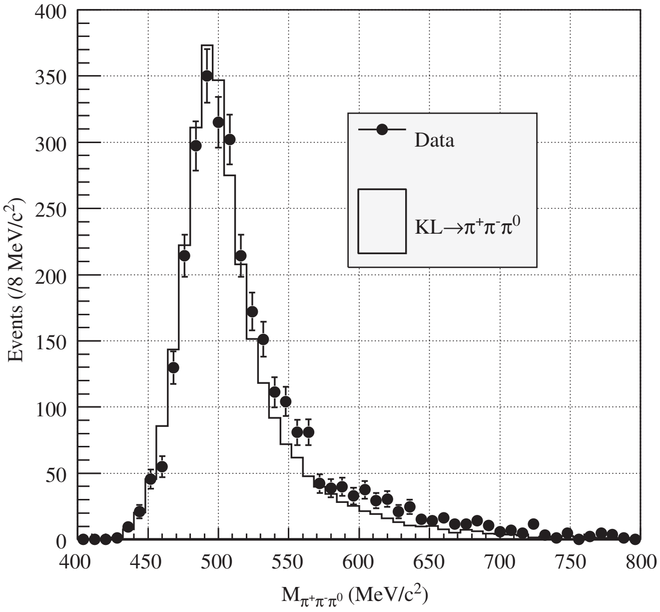

Fig. 7. Invariant mass distribution of $\pi^+\pi^-\pi^0$ after imposing all the kinematical cuts except the cut on $M_{\pi^+\pi^-\pi^0}$. Dots with bars indicate the data and a histogram shows the $K_L^0 \to \pi^+\pi^-\pi^0$ signals from the simulation result.

Table 6
Summary of the kinematical cuts. Here the results in the Ni target runs are shown. N_{pass} indicates the number of events which passed the cut given in the row. Reduction here is defined by normalizing to the number of events after the primary event selection.

Cut name	Condition	N_{pass}	Reduction (%)
Primary event selection		12 059	–
π^0 invariant mass	$105 < M_{\gamma\gamma} < 165\ \mathrm{MeV}/c^2$	5801	48
Azimuthal angle	$\lvert\Delta\phi_\pm\rvert < 168^\circ$ or $\lvert\Delta\phi_\pm\rvert > 192^\circ$	3465	29
$\pi_\pm$ momentum	$p_\pm > 0$	2871	24
Vertex position	$21.0 < z_v < 23.5$ m	2722	23
Two photon distance	$d_{2\gamma} > 40$ cm	2666	22
K_L^0 invariant mass	$460 < M_{\pi^+\pi^-\pi^0} < 540\ \mathrm{MeV}/c^2$	1923	16

4. Results and discussions

4.1. K_L^0 flux

The number of K_L^0s at the exit of the beam line was taken as a measure of the flux. The flux was normalized to 2×10^{14} protons on the production target (POT), which corresponds to the designed value of POT per single spill from the MR accelerator of J-PARC with the slow extraction.

In order to determine the flux at the exit of the beam line from the observed K_L^0 decays, the geometrical acceptance and the analysis efficiencies must be evaluated, as well as the decay probability and the $K_L^0 \to \pi^+\pi^-\pi^0$ branching ratio. The efficiencies of the hodoscope planes were evaluated by data taken with a special trigger, and were found to be 98.4% per plane in average. Hits were required in all the eight planes and thus the total efficiency was estimated to be 87.4%. The average live time of the data acquisition was 97.7% during the runs. The decay probability, geometrical acceptance, and analysis efficiencies were evaluated by the MC simulations to be 5.6%, 0.079%, and 14.4%, respectively. Note that these values depend on the K_L^0 momentum distribution, as discussed later. The values obtained with our resultant spectra were used.

Information from a secondary emission chamber (SEC) in the proton extraction line of the MR was used to monitor the POT value in each spill. The SEC provided a scaler count proportional to the proton intensity. It was normalized so as to agree with the measured intensity by a current transformer (CT) in the MR, provided by the accelerator group. The beam loss at the extraction was 1.4% according to measurements by loss monitors, and was taken into account in the calculation.

By using the $K_L^0 \to \pi^+\pi^-\pi^0$ branching ratio of 12.54% [19], the K_L^0 yields for the Ni and Pt targets were obtained as listed in Table 7.

Compared with the MC simulations, the resultant K_L^0 flux for the Ni target was consistent with the expectations from GEANT3 and FLUKA but larger than that from GEANT4. For the Pt target, the measured value was larger than all the expectations by three simulation packages. Note that the differences among various MC simulations include the effects of scattering from the 7-cm-thick lead absorber, as well as the K_L^0 production cross-section. We also examined the ratio of the K_L^0 yield of the Pt target to that of the Ni target. The measurements gave the value of $2.16^{+0.38}_{-0.36}$, while the expectations were 2.05 by GEANT4, 1.58 by GEANT3, and 1.56 by FLUKA, respectively.

4.2. K_L^0 momentum spectrum

Fig. 8 shows the reconstructed K_L^0 momentum distribution for the Ni target. The distribution includes the detector acceptance and

Table 7
Resultant K_L^0 flux at the exit of the beam line. The K_L^0 yields for the Ni and the Pt targets and their ratio were summarized, together with the expectations by MC simulations. The first uncertainties are statistical and the second ones are systematic (discussed in Section 4.3).

Target	Flux (normalized to 2×10^{14} POT)			
	Data	GEANT4	GEANT3	FLUKA
Ni (5.4-cm-long)	$(1.94 \pm 0.05^{+0.25}_{-0.24}) \times 10^7$	0.74×10^7	1.51×10^7	2.07×10^7
Pt (6.0-cm-long)	$(4.19 \pm 0.09^{+0.47}_{-0.44}) \times 10^7$	1.52×10^7	2.38×10^7	3.24×10^7
Pt/Ni ratio	$2.16^{+0.38}_{-0.36}$	2.05	1.58	1.56

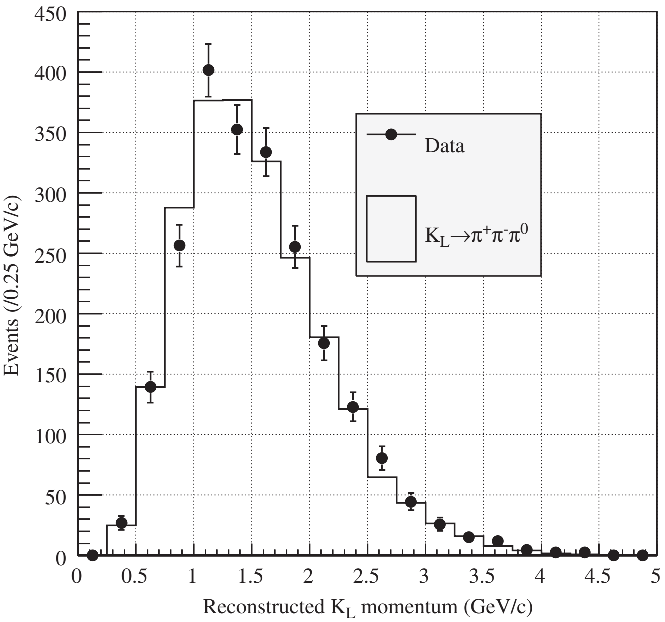

Fig. 8. Reconstructed K_L^0 momentum distribution after imposing all the kinematical cuts. The dots indicate data with statistical errors. The histograms show the MC expectations for the signal and possible remaining backgrounds. Note that the resultant K_L^0 yield and spectrum by this measurement were used in the simulation.

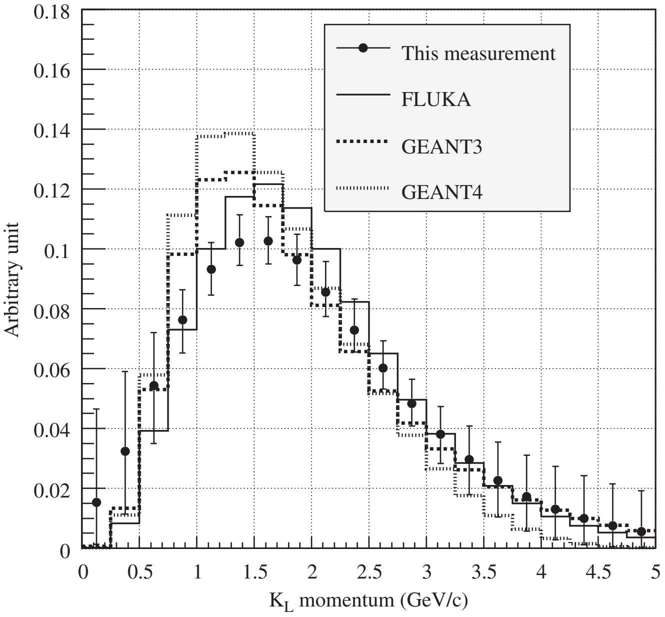

Fig. 9. K_L^0 momentum spectrum at the exit of the beam line. Points indicate the resultant spectrum with one standard-deviation error bars. The deviations in the bins are correlated with each other. The histograms show the simulation results by FLUKA, GEANT3, and GEANT4, respectively. All the distributions are normalized to be 1 when integrated.

analysis efficiencies, as well as the decay probability in the fiducial region. To obtain the K_L^0 momentum spectrum at the exit of the beam line, the expected distribution was calculated from a given K_L^0 spectrum and compared with the measured distribution. The simulation included effects of detector resolutions. The result was fed back to the K_L^0 spectrum iteratively to minimize the difference. Fig. 9 shows the resultant K_L^0 momentum spectrum at the exit of the beam line, with overlays of various MC expectations.

Table 8
Summary of systematic uncertainties.

Source	Uncertainties (%)	
	Ni target	Pt target
Cut effectiveness	±12.2	±10.4
K_L^0 momentum distribution	$+3.5/-1.1$	$+4.2/-0.2$
Others	±1.4	±1.3
Total	$+12.8/-12.3$	$+11.3/-10.5$

As seen in the figure, the data have a slightly broader spectrum than those from the simulations.

4.3. Systematic uncertainties

Estimates of the systematic uncertainties are listed in Table 8. The largest uncertainty comes from “cut effectiveness”. In reality, the effectiveness of various kinematical cuts differed from those expected by the MC simulations. We considered the differences to be sources of systematic uncertainties, and took them into account in the following way. A partial acceptance, A_i, was defined by

$$A_i = \frac{N\ (\text{all the cuts applied})}{N\ (\text{all but the } i\text{–th cut applied})} \tag{3}$$

where the index i denotes one of the kinematical cuts listed in Table 6, and N is the number of remaining events after applying the cuts specified in the parentheses. We compared the values of A_i obtained with the real data and the MC data; the fractional differences between the two were considered to be the systematic uncertainties. These fractional differences were summed in quadrature. This systematic uncertainty resulted in 12.2% for the Ni and 10.4% for the Pt target, respectively.

The second largest systematic uncertainty originated from uncertainties in the K_L^0 spectrum. As stated in the previous subsection, the momentum spectrum was necessary as an input for calculating the acceptance. The obtained spectrum shown in Fig. 9 has statistical uncertainties. The variation of the acceptance based upon the statistical fluctuations of the momentum spectrum was studied with MC simulations. These systematic uncertainties resulted in $+3.5/-1.1\%$ for Ni and $+4.2/-0.2\%$ for the Pt target, respectively.

Other systematic uncertainties due to the alignment errors of the detector or uncertainties in the background estimations and the POT values were found to be small, as shown in Table 8. Summing up all the contributions in quadrature, the systematic errors amounted to be $+12.8/-12.3\%$ for Ni and $+11.3/-10.5\%$ for the Pt target, respectively.

5. Summary

In this paper, we have described the results of K_L^0 flux measurements carried out at the newly built neutral-kaon beam line of the J-PARC Main Ring accelerator. The primary proton energy was 30 GeV and the K_L^0 production angle and the solid angle of the beam line were 16° and 7.8 μsr, respectively. The K_L^0 flux and spectrum were measured by counting $K_L^0 \to \pi^+\pi^-\pi^0$ decays with a simple setup consisting of an electromagnetic calorimeter and a tracking hodoscope system. The K_L^0 yields at the exit of the beam line, normalized to 2×10^{14} POT, were obtained to be 1.94×10^7 for 5.4-cm-long Ni target and 4.19×10^7 for 6-cm-long Pt target, respectively. The measured K_L^0 flux was consistent with or larger than the values predicted by the MC simulations, and its momentum spectrum was somewhat wider than the predictions. These results provide new data of the K_L^0 production with 30-GeV protons at a large angle, and comparisons with the simulations are useful for future designs of rare K_L^0 decay experiments.

Acknowledgment

We would like to express our gratitude to all members of the J-PARC accelerator and Hadron Beam groups for their support. This research was partially supported by Grant-in-Aid for Scientific Research on Priority Areas from the Ministry of Education, Culture, Sports, Science and Technology in Japan. Some of the authors were supported by Grant-in-Aid for JSPS Fellows from the Japan Society for the Promotion of Science or by a U.S. Department of Energy Grant DE-SC0002644.

References

[1] L.S. Littenberg, Physical Review D 39 (1989) 3322;
A.J. Buras, S. Uhlig, F. Schwab, Reviews of Modern Physics 80 (2008) 965 (and reference therein).
[2] L. Wolfenstein, Physical Review Letters 51 (1983) 1945.
[3] M. Kobayashi, T. Maskawa, Progress of Theoretical Physics 49 (1973) 652.
[4] J. Brod, M. Gorbahn, E. Stamou, Physical Review D 83 (2011) 034030.
[5] J.K. Ahn, et al., E391a Collaboration, Physical Review D 81 (2010) 072004.
[6] ⟨http://j-parc.jp⟩; Y. Yamazaki, et al., KEK Report No. 2002-13, JAERI-Tech 2003-44 and J-PARC-03-01, 2003.
[7] J. Comfort, et al., E14 Collaboration, Proposal for $K_L^0 \to \pi^0 \nu \bar{\nu}$ Experiment at J-Parc, ⟨http://j-parc.jp/NuclPart/Proposal_e.html⟩.
[8] T. Shimogawa, et al., E14 Collaboration, Nuclear Instruments and Methods in Physics Research Section A 623 (2010) 585.
[9] G. Takahashi, et al., Japan Journal of Applied Physics 50 (2011) 036701.
[10] GEANT4 version 9.4 patch-02, ⟨http://geant4.cern.ch⟩; S. Agostinelli, et al., Nuclear Instruments and Methods in Physics Research Section A 506 (2003) 250; J. Allison, et al., IEEE Transactions on Nuclear Science NS-53 (2006) 270.
[11] GEANT3, A Detector Description and Simulation Tool, Application Software Group, Computing and Networks Division, CERN, Geneva, 1993; A. Fasso, A. Ferrari, J. Ranft, P.R. Sala, in: A. Menzione, A. Scribano (Eds.), Proceedings of the IV International Conference on Calorimetry in High Energy Physics, La Biodola, World Scientific, 1993, pp. 493–502.
[12] FLUKA Version 2008.3 and Later, ⟨http://www.fluka.org/fluka.php⟩; G. Battistoni, et al., in: M. Albrow, R. Raja (Eds.), Proceedings of the Hadronic Shower Simulation Workshop 2006, AIP Conference Proceeding, vol. 896, 2007, pp. 31–49; A. Fasso, A. Ferrari, J. Ranft, P.R. Sala, CERN-2005-10, 2005, INFN/TC_05/11, SLAC-R-773.
[13] D.E. Jaffe, K.H. Lo, J.R. Comfort, M. Sivertz, Nuclear Instruments and Methods in Physics Research Section B 246 (2006) 309.
[14] Hamamatsu Photonics Inc., ⟨http://jp.hamamatsu.com/⟩.
[15] M. Doroshenko, et al., E391a collaboration, Nuclear Instruments and Methods in Physics Research Section A 545 (2005) 278.
[16] Eljen Technology, ⟨http://www.eljentechnology.com/⟩.
[17] Kuraray Co., Ltd., ⟨http://www.kuraray.co.jp/en/⟩.
[18] The electronics we used for the hodoscope was originally developed for the SciBar detector in the long baseline neutrino oscillation experiment at KEK (K2K); K. Nitta, et al., Nuclear Instruments and Methods in Physics Research Section A 535 (2004) 147; M. Yoshida, et al., IEEE Transactions on Nuclear Science NS-51 (2004) 3043.
[19] K. Nakamura, et al., Particle Data Group, Journal of Physics G 37 (2010) 075021.